7.1 DETERMINING WINTERTIME HETEROGENEOUS PACK ICE CHARACTERISTICS AND THEIR IMPACT ON THE AGGREGATE ATMOSPHERIC SURFACE FLUXES

P. O. G. Persson[1], E. L Andreas[2], J.-W. Bao[4], C. W. Fairall[4], A. A. Grachev[1], P. S. Guest[3], and R. E. Jordan[2]
[1]CIRES/NOAA/ETL, Boulder, Colorado
[2]U.S. Army Cold Regions Research and Engineering Laboratory, Hanover, New Hampshire
[3]Naval Postgraduate School, Monterey, California
[4]NOAA/ETL, Boulder, Colorado

1. INTRODUCTION

Overland et al. (2000) showed histograms of AVHRR-derived surface temperatures (T_s) over the Arctic pack ice during clear-sky wintertime conditions. These histograms were remarkable in that they showed a range of T_s of up to 19°C (-42° to -23°C) within a 100 X 100 km area centered on the Surface Heat Budget of the Arctic Ocean (SHEBA) site. This study also showed that surface sensible heat fluxes (H_s) aggregated over this area are 5-12 W m^{-2} greater than those measured at the SHEBA site during these clear-sky conditions because of the areas of higher T_s. Questions motivated by the Overland et al. results include: 1) is this large T_s range over such a small area physically realistic? 2) if so, what is the spatial distribution of the warm and cold areas and what are the implications of this distribution?, 3) are the clear-sky T_s and H_s variations representative of the variations during cloudy conditions?, 4) is there another method that can show the spatial distribution of T_s and H_s during cloudy conditions so long-term mean aggregate T_s and H_s values can be computed?

In this study, we develop a method to estimate the wintertime aggregate T_s and H_s under all sky conditions. The method combines synthetic aperture radar (SAR) data and a simple one-dimensional snow and ice model. The SAR data show the time of the formation of first-year ice (FYI), the size of the FYI areas, and their subsequent movements. The 1-D model provides the evolution of the ice thickness, snow depth, T_s, and H_s for freezing leads. In addition to providing estimates of aggregate T_s and H_s, the technique can provide the spatial distribution of ice thickness and snow depth necessary for 3-D mesoscale simulations to explore other aggregation techniques and the flux contribution of mesoscale circulations resulting from the larger scales of surface heterogeneity. Ice that forms in leads during the 9-month freezing season is known as FYI, whereas ice that survives the summer melt season is defined as multi-year ice (MYI).

This paper describes the structure and validation of the 1-D snow and ice model, the use of SAR data for identifying FYI generation and movements, and the combination of these to provide surface fields of T_s and H_s and hourly time series of aggregate values. Aggregate values from the SAR/1-D model technique and the AVHRR measurements are compared with each other and with those from the long-term SHEBA site on multi-year ice (MYI). Results from preliminary simulations with the Penn State/NCAR Mesoscale Model (MM5) using a 3-D version of the snow and ice model will be presented at the conference, allowing a comparison of aggregate-scale fluxes using various methods.

Corresponding author address: Dr. Ola Persson, CIRES/NOAA/ETL, R/ET7, 325 Broadway, Boulder, CO 80305; e-mail: opersson@cires.colorado.edu

2. ONE-DIMENSIONAL SNOW AND ICE MODEL

2.1 *Description*

The snow and ice model is based on that by Semtner (1976), which is a simplification of that used by Maykut and Untersteiner (1969). A principal difference in our model is that both the snow and ice are represented by multiple layers rather than just the ice. The model solves the basic heat equation

$$(\rho c)_n \frac{\partial T}{\partial t} = k_n \frac{\partial^2 T}{\partial z^2}$$

where T is the temperature, z is the depth, k_n, is the thermal conductivity, t is time, and $(\rho c)_s$ is the volumetric heat capacity for ice (n = i) and snow (n = s). At the snow-ice interface, the heat flux,

$$F_n = k_n \frac{\partial T}{\partial z}$$

is continuous so

$$k_s \left.\frac{\partial T}{\partial z}\right|_s = k_i \left.\frac{\partial T}{\partial z}\right|_i$$

and

k_s = 0.33 W m^{-1} K^{-1},
$(\rho c)_s$ = 6.0 x 10^5 J m^{-3} K^{-1}.
k_i = 2.00 W m^{-1} K^{-1},
$(\rho c)_i$ = 2.43 x 10^6 J m^{-3} K^{-1}.

The change in the surface temperature from time step t-1 to time step t is computed assuming a surface energy balance leading to the relations

$$T_s^t = T_s^{t-1} + \Delta T_s ,$$

where

$$\Delta T_s = \Big[-\varepsilon_s \, \sigma \left(T_s^{t-1}\right)^4 + \varepsilon_s \, F_{LW} + (1-\alpha) F_{SW} - \left(H_s + H_l\right) + 2k_n \left(T_{1n} - T_s^{t-1}\right) / h_{1n} \Big] / \Big[-4\varepsilon_s \sigma \left(T_s^{t-1}\right)^3 - 2k_n / h_{1n} - \rho_a c_p C_H u_a \Big] \quad (1)$$

and F_{LW} (F_{SW}) is the incoming longwave (shortwave) radiation, α is the albedo, H_s (H_l) is the turbulent sensible (latent) heat flux, T_{1n} is the temperature in the top snow or ice layer, h_{1n} is the thickness of that layer, ε_s is the emissivity of the snow or ice surface (= 0.99), σ is the Stefan-Boltzmann constant, ρ_a is the air density, c_p is the specific heat of air at constant pressure, C_H is the turbulent heat transfer coefficient, and u_a is the wind speed at 10 m. The last term in the denominator in (1) comes from the expression for H_s. A similar expression from H_l is small and has been ignored. Each time step, (1) is iterated up to 5 times to obtain greater accuracy. Though (1) forces an immediate energy balance at the surface, it does not conserve energy in the top layer. We have used a typical effective value for k_s since the measured one appears to be low when considering the net surface energy flux (Sturm et al. 2002a).

The bottom ice temperature is assumed to remain constant at the freezing point of sea ice (-1.8°C), and no ocean heat flux is specified. Following Ebert and Curry (1994) and Schwarzacher (1959), the latent heat of fusion at the bottom of the ice is ~12% less than elsewhere because of the large amount of brine initially retained, enhancing the wintertime ice growth.

The number of snow layers is variable but is maximized dependent on the snow depth and the following criteria:

1) no snow layer is shallower than 2 cm,
2) the top layer is 2 cm thick if at least 4 cm of snow exists,
3) the remaining snow depth is divided equally among the other layers,

and

4) a maximum of 5 snow layers is permitted.

The first criterion is needed to permit reasonable time steps for numerical stability while the second criterion is needed for rapid temperature response and proper interaction with the atmosphere. For the ice, an ice cover is assumed to exist if it is at least 2 cm thick, no ice layer is thinner than 2 cm, and the ice pack is equally divided among the ice layers, with a maximum of 5 ice layers permitted. Each time step, the vertical structure is checked for these criteria and regridded if necessary.

2.2 *Validation*

2.2.1 Simulation design

The performance of the 1-D code was tested at the Pittsburgh MYI site, which was near the main SHEBA camp and about 100 m from the Atmospheric Surface Flux Group (ASFG) tower (see Fig. 1 of Persson et al. 2002), and at the Baltimore FYI site about 6 km from the main SHEBA site. Measurements of snow/ice temperature profiles and snow/ice thickness measurements are available from these sites (Perovich et al. 2003). The Pittsburgh site had an ice thickness of 1.75 m on YD305 (Nov. 1), the date of the model initialization. The FYI at Baltimore was a frozen late-summer lead, so ice was already 0.52 m thick by YD305. The initial ice and snow temperature profiles are taken from the observations for the model validation runs.

The hourly forcing at both the MYI and the FYI regions is assumed to be represented by the measurements of incoming longwave and shortwave radiation, 10-m wind speed, and 10-m air temperature at the ASFG site. Hourly precipitation estimates were obtained by using the calibrated daily precipitation measurements from the Nipher shielded snow gauge at the SHEBA Project Office (SPO) site (Uttal et al. 2002) to calibrate reflectivity-snowfall (Z-S) relationships using hourly reflectivity values from the SHEBA cloud radar (e.g., Intrieri et al. 2002). Using a snow density of 100 kg m^{-3} to convert the precipitation liquid-water to snow depth, this precipitation time series was able to account for the observed increase in snow depth at both Baltimore and Pittsburgh (Fig. 1) if a reduction of 4 cm is assumed to occur at Pittsburgh due to wind scouring associated with two observed changes in wind direction. The assumption of spatially uniform 10-m wind speed and air temperature, also made by Overland et al. (2000), will be assessed using the mesoscale model.

Over the MYI, the surface heat fluxes are calculated using the COARE surface flux

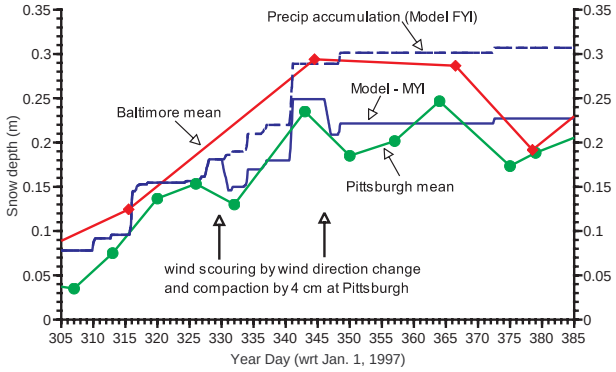

Fig. 1: Snow depth as a function of time from accumulated precipitation (blue-dashed)(used in model for FYI), Baltimore and Pittsburgh observations (red and green solid, respectively), and the adjusted accumulated precipitation used in the model at the Pittsburgh MYI site.

parameterization (Fairall et al. 1996; 2003) but using the Reynolds number formulations over snow of Andreas (1987) and the stability correction terms for stable conditions of Beljaars and Holtslag (1991). Later versions will use the stability correction terms derived from the ASFG tower data (Grachev et al. 2004). Over the areas of FYI, which are assumed to be much smaller than the MYI areas, the heat transfer coefficients (C_H) are assumed to be the same as those over the MYI at the same time. This is tantamount to assuming that turbulence intensity over the FYI does not have time to change as the air flows from the MYI to the FYI and then back over the MYI. The fluxes, however, will be impacted as the T_s over the FYI are warmer than those over the MYI. As discussed by Overland et al. (2000), this assumption probably underestimates the true transfer coefficient, so comparisons will be made assuming a constant but generally larger $C_H = 1 \times 10^{-3}$ and a C_H computed from the COARE scheme using the local stability. The latter assumption may be valid over the largest FYI areas.

2.2.2 Validation results

The main 1-3 day temperature variations observed within the pack ice during the 81-day test period (YD305-386) are captured by the 1-D model (Fig. 2), with the variations damping with increasing depth in the ice. In both the observations and the model, a large thermal gradient is frequently present across the snow pack. The ice thickness grows as well, increasing from 1.75 m to 2.15 m in the model and 2.08 m in the observations.

The modeled T_s time series (Fig. 3a) has correlation coefficients of $r^2 = .982$ - .983 with the

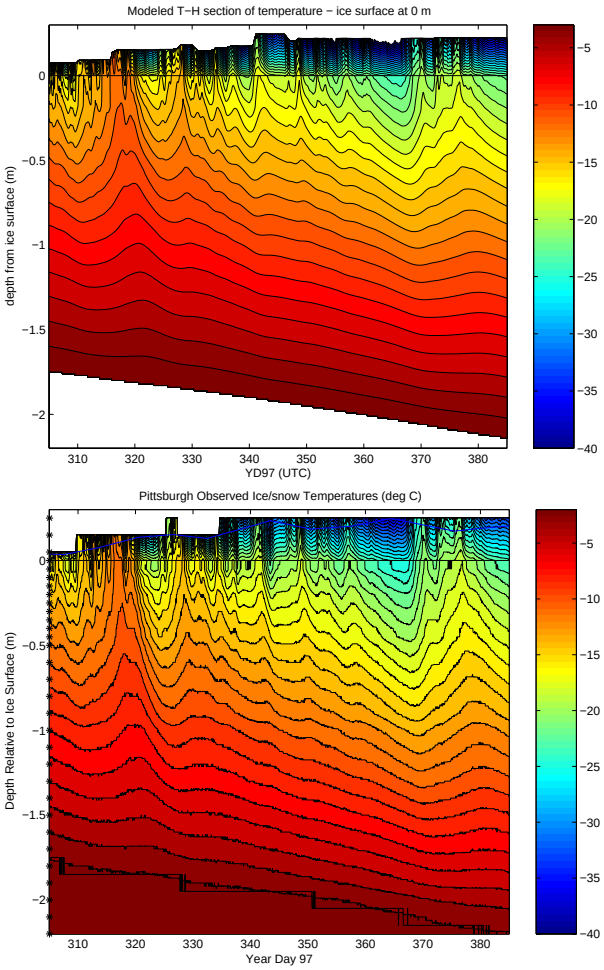

Fig. 2: Temperature time-height sections in the snow and ice at Pittsburgh from a) the 1-D model and b) the Pittsburgh observations. The top of the ice is at 0 m. In b), the stair-step line marks the bottom of the ice and the stars show the measurement levels.

Pittsburgh and ASFG T_s (T_{s_Pitt} and T_{s_ASFG}). The time series show that the modeled T_s are in excellent agreement with T_{s_Pitt} before YD342 (Dec. 8) and tends to be 1-2°C colder than the observations during clear-sky periods afterwards. YD342 marks the end of the last significant period of snow accumulation (Fig. 1) and the end of a strong wind period (e.g., Uttal et al. 2002). The T_{s_ASFG} is typically slightly colder than the T_{s_Pitt} during clear skies because of the deeper snow at the ASFG tower. At the Baltimore FYI site (not shown), similar excellent correlations (r^2 = .980-.988) with the observed T_s were found, though here the model tended to be in excellent agreement before YD338 (Dec. 4) and 1-3°C colder during the clear- sky periods after YD338. The modeled H_s (Fig. 3b) has a r^2=0.764 with the observed H_s at the ASFG site. This "lack of perfection" is due to using the COARE flux

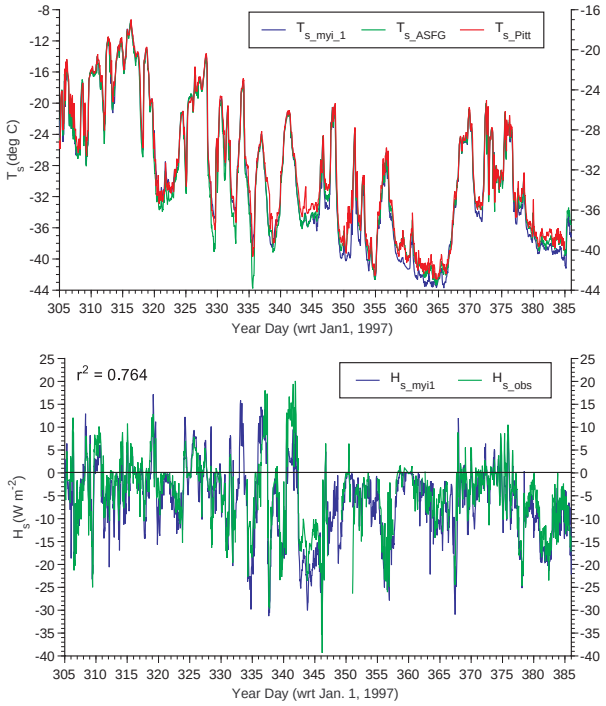

Fig. 3: Time series of modeled and observed a) surface temperature and b) H_s at the Pittsburgh or ASFG site.

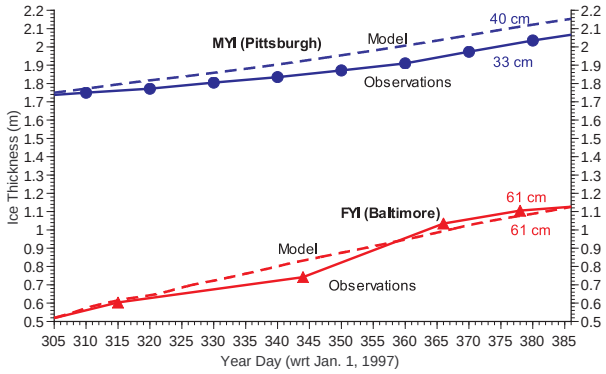

Fig. 4: Modeled and observed ice thicknesses at the Pittsburgh (MYI) and Baltimore (FYI) sites.

scheme rather than the observed H_s. A simulation using the observed H_s at the MYI site had only negligible differences in T_s and ice growth. At the Pittsburgh site, the ice thickness growth error is about 7 cm out of the 40 cm of growth that occurred (Fig. 4). At the Baltimore FYI site, the model reproduced the observed ice growth of 61 cm, though the modeled ice growth rate had less variability than the observed one.

The Overland et al. (2000) study suggests that T_s and H_s will be greater over the FYI than over the MYI. Here we test whether this is true for the relatively thick Baltimore FYI (0.52-1.12 m) and not thinner FYI regions generated during the winter. Observations show that T_s is consistently 0

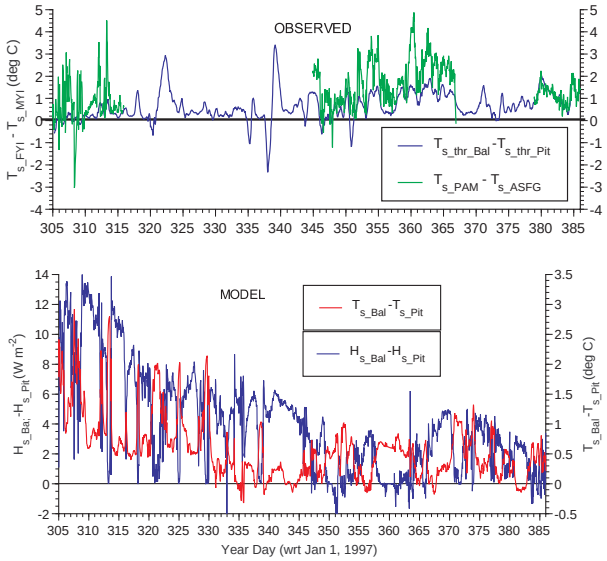

Fig. 5: a) Observed T_s differences between the Baltimore and Pittsburgh thermistor strings (blue) and the radiative T_s values from the Baltimore PAM station and the ASFG site (green). b) Modeled differences between the FYI and MYI sites of T_s (red) and H_s (blue).

- 2°C greater (averaging 0.6°C) at the Baltimore FYI site than at the MYI site of the main SHEBA camp (Fig. 5a). The model shows T_s consistently greater by 0 to 1.5°C (averaging 0.6°C) on the FYI compared to the MYI (Fig. 5b). This difference in T_s produces H_s that are greater by 0-13 Wm^{-2} (averaging 3.9 W m^{-2}) on the modeled FYI. Hence, since the observations and the model show similar T_s differences, it is likely that the model H_s differences are real. No reliable H_s values are available from the Baltimore Flux- Portable Automated Mesonet (PAM) station during this time period to validate this.

Note that the modeled T_s differences decrease with time, as is physically consistent with an increasing snow depth and ice thickness. However, it is unknown why the observations show a slight increase in T_s differences rather than the expected decrease.

2.2.3 Sensitivity tests

Tests were done on both the MYI and FYI sites to examine the sensitivity of the 81-day mean T_s, H_s, heat transfer coefficient (C_H), and ice growth (Δz_i) to the H_s calculation method. The methods tested included using the a) observed H_s (only for the MYI site), b) COARE scheme with local stability, c) MYI C_H value, and d) constant C_H = 1 $X10^{-3}$ (only at the FYI site). At the MYI site, the mean T_{s_MYI} only varied from -29.9°C to -29.6°C (mean T_{s_Pitt} = -28.6°C), the mean H_{s_MYI} varied from -6.1 W m^{-2} to -5.3 Wm^{-2} (mean H_{s_obs} =

-4.6 W m^{-2}) and Δz_{i_MYI} varied from 40.3 cm to 40.7 cm (Δz_{i_Pitt} = 33 cm). At the FYI site, the mean T_{s_FYI} varied between -29.0 and -28.6°C (mean T_{s_Bal} = -28.0°C), the mean H_{s_FYI} varied between -3.6 and -2.2 W m^{-2}, and the Δz_{i_FYI} varied between 59.9 and 60.6 cm (Δz_{i_Bal} = 61 cm). The mean C_H for the three methods on the FYI only ranged from 0.91 X 10^{-3} (MYI C_H value) to 1.03 X 10^{-3} (COARE scheme with local stability). The observed mean C_H at the MYI site was 0.87 X 10^{-3}, and the COARE scheme on the MYI yielded a mean C_H = 0.90 X 10^{-3}. With such small variations, we conclude that the ice at the Baltimore FYI site is too thick to produce enough variability to reliably test the best flux-calculation method for heterogeneous ice.

Decreasing the initial snow depth on the MYI by 4 cm increased the modeled mean T_s by 0.3°C and the clear-sky T_s by 0.5-1.0°C, but also increased the already high Δz_i by 2.7 cm. This test does show that the insulating effect of the snow impacts the clear-sky T_s. Increasing the latent heat of fusion at the bottom of the ice (i.e., ignoring the brine content) had little impact on the mean T_s and H_s, but did reduce the ice growth by 7.2 - 9.6% (3.9 cm on the MYI and 5.8 cm on the FYI).

2.2.2 Validation conclusions

The above diagnostics give us confidence that the simple 1-D snow/ice model produces realistic evolutions of the T_s and the ice thickness. However, none of the sensitivity studies totally explain the model's 1) 1-3°C cold bias during clear skies after YD338-342 (Dec. 4-8) and 2) the 17% excess ice growth on the MYI. The first problem is probably due to the omission of a process that is making the snow cover less insulating near Dec. 8, as suggested by its sensitivity to the snow depth. Indeed, Sturm et al. (2002b), note that the snow layer deposited at SHEBA from Dec 1 - 8 was accompanied by strong winds producing a "fine-grained, dense, well-bonded type of snow with high thermal conductivity." This conductive snow "formed during storms when snow grains were tumbled by the wind, breaking them and producing smaller grains which packed together." Hence, a temporally variable k_s allowing for such processes might help the model's cold bias. The latter problem may partly be explained by the ad hoc use of a lower latent heat of fusion at the ice bottom (though we will continue using this in the remainder of this study), or it might be improved by the inclusion of an ocean heat flux.

3. SPATIAL HETEROGENEITY

3.1 FYI Formation, Ice Thickness and Snow Depth

Automated post-processing of SAR data from the Canadian RADARSAT satellite can clearly distinguish the signature of MYI and FYI by the backscatter intensity (Kwok et al. 1992; Kwok and Cunningham 1994), with erroneous classification of less than 6% (Fetterer et al. 1994). The magnitude of the backscatter of the C-band SAR depends on the large and small-scale roughness and the dielectric properties of the surface. For the subfreezing pack ice, the backscatter is a complex expression of the properties of the snow cover, the large and small-scale surface roughness of the snow-ice interface, the ice salinity, and the characteristics of the inhomogeneities (e.g., air bubbles, crystal size) in the ice volume. SAR images from the RADARSAT satellite are available generally every 1-6 days over the Western Arctic Ocean at a nominal resolution of 100 m (Kwok and Cunningham 2002). These images are created by averaging the full 30 m resolution images, thereby making speckling insignificant in the low-resolution images.

The ability to distinguish between MYI and FYI and the temporal and spatial resolution of the data allow the possibility of detecting the time and location of the creation of a FYI signature within the MYI (Kwok et al. 1995). While it is not possible with confidence to state whether a FYI pixel is open water or another subcategory of FYI, the primary physical mechanism by which FYI can replace MYI is by the opening of a lead which subsequently freezes over time. SAR data from SHEBA was examined for times and locations of FYI formation, and these FYI features were tracked in time. Only the main FYI features were tracked and complications of frost-flower formation and ice flooding were ignored unless other information was available.

Figure 6 shows a sequence of SAR images of the SHEBA site from Nov. 7, 1997, to Jan. 20, 1998. On Nov. 7, most of the area is covered by the high-reflectivity MYI, with only a few small areas of dark-colored FYI near the bottom of the image. A 50 X 50 km square is centered on the SHEBA ship. The vertices of this square are tracked in time by following backscatter features, showing the displacement and deformation (rotation, shear, and divergence) of the ice (Kwok and Cunningham 2002; Stern and Moritz 2002; Lindsay 2002), and allowing the temporal tracking of the area of FYI within the polygon. By YD338 (Dec. 4), the square

has deformed to a polygon, and some FYI is present within and outside this polygon. The next image in the SAR sequence, taken 6 days later (Dec. 10), shows a large increase in FYI within the polygon to the west of the SHEBA site and outside the polygon as well. This new FYI is assumed to have formed on YD340 (Dec. 6) and will be referred to as FYI0 (Table 1). Three SAR frames and 10 days later (YD354, Dec. 20), a larger area of FYI is present within the polygon, but just to the south of the polygon the area of FYI has increased substantially. Much of this FYI is very low reflectivity, and appears to have been a lead that opened on YD353 (Dec. 19) (i.e., between YD352 and YD354). We will refer to the FYI formed on YD353 as FYI1.

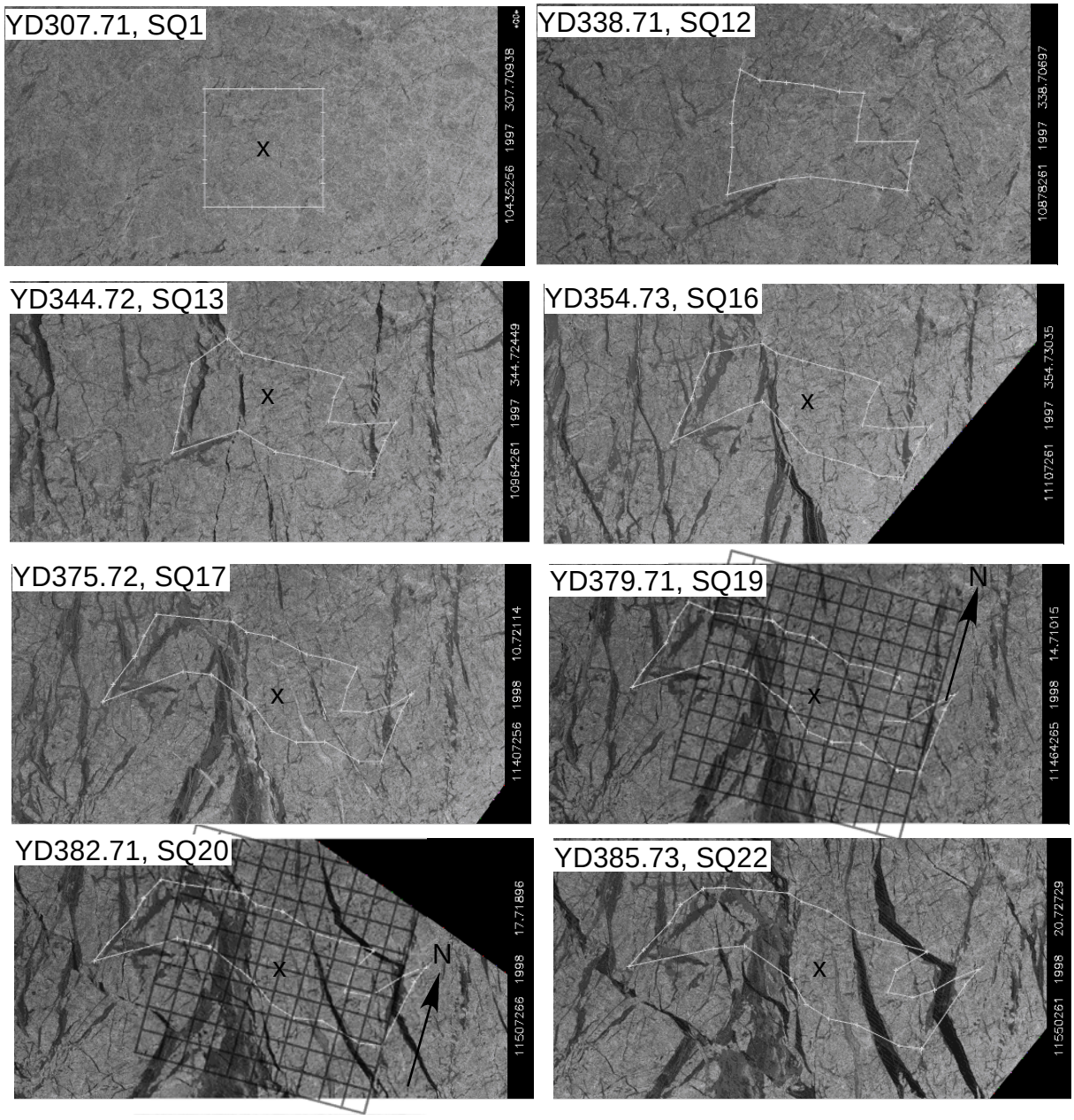

Fig. 6: SAR backscatter images from Nov. 7, 1997, to Jan. 20, 1998, near the SHEBA site (marked by "x"). A 50 X 50 km cell centered on the SHEBA ship is shown in the first image, and the vertices of this cell are tracked in subsequent images to show the deformation. The year day and the sequence number are shown in the upper left corner for each image. The thicknesses corresponding to the four FYI regions discussed in the text are also identified on the histograms. A 100 km X 100 km grid overlays the images on Jan. 14 and 17.

Table 1. *The formation time of various FYI regions discussed in the text, and their spatial relative frequency (from the SAR image processing in the 100X110 km area centered on the SHEBA site), and ice thickness, and snow depth (cm; from the 1-D model) on specific dates. Also shown are the values for the multi-year ice (MYI).*

	FYI0	**FYI1**	**FYI2**	**FYI3**	**FYI4**	**MYI**
Date formed	YD340 Dec. 6 00 UTC	YD353 Dec. 19 00 UTC	YD376 Jan. 11 00 UTC	YD381 Jan. 16 00 UTC	YD383 Jan. 19 00 UTC	N/A
Date						
Rel. Frequency						
YD354	0.019	0.145	0	0	0	0.836
YD375	0.019	0.145	0	0	0	0.836
YD376	0.025	0.188	0.034	0	0	0.753
YD379	0.025	0.188	0.034	0	0	0.753
YD382	0.022	0.182	0.032	0.044	0	0.720
YD385	0.022	0.189	0.021	0.054	0.038	0.676
Ice thickness						
YD354	34	7	-	-	-	198
YD375	66	64	-	-	-	209
YD376	67	65	3	-	-	210
YD379	70	70	16	-	-	212
YD382	74	76	28	10	-	213
YD385	78	83	38	23	8	215
Snow depth						
YD354	10	2	-	-	-	22
YD375	11	3	-	-	-	23
YD376	11	3	2	-	-	23
YD379	11	3	2	-	-	23
YD382	11	3	2	2	-	23
YD385	11	3	2	2	2	23

A 3-week gap in SAR images occurred between Dec. 20 and Jan. 10. Fortunately, the deformation of the ice was not large during that period, with most ice features on Dec. 20 being readily recognizable on Jan. 10, though a substantial widening of the FYI regions occurred within and south of the polygon. Between YD375 and YD376 (Jan. 10 and Jan. 11), leads formed within the FYI to the west and south of the SHEBA site within and outside the polygon and are evident on the image from YD379 (Jan. 14). This FYI forming on Jan. 11 will be called FYI2. A linear region of bright reflectivity is evident on Jan. 10 just SE of the SHEBA ship. The temporal evolution of the backscatter from this region suggests that this is a lead with frost flowers forming on thin ice (Stern and Moritz 2002), and is therefore considered to be part of FYI2. Hence, the FYI1 and FYI2 provide areas of relatively thin ice with widths of 7-15 km at ranges of 20-50 km to the west and south from the SHEBA site. Near 00Z Jan. 16, significant deformation occurs from SW through SE to NE of the SHEBA site, opening numerous leads both within existing FYI as well as in the MYI, as is seen on the SAR image from Jan. 17. Thin ice areas of several kilometers in width are present between 15-40 km from the SHEBA site from NNE through SE to W. The FYI forming at 00Z Jan. 16 is referred to as FYI3. The deformation continued fairly steadily until Jan. 24, producing thin FYI in many areas of the domain, as can be seen by the SAR image from Jan. 20. The thin ice formed during this last period is referred to as FYI4.

The SAR images of Jan. 10, 14, 17, and 20 were processed to identify the pixels associated with the MYI and the five FYI categories. The processing involved automated intensity thresholding, statistical grouping, and subjective modification of the automated pixel selections to produce a spatial distribution of each ice category that was consistent with the evolution evident in the image sequence and the previous discussion.

This processing led to the identification of pixels assigned to each of the ice categories and determination of the relative percentages shown in Table 1. Figure 7 shows the spatial distribution of

this pixel-classification processing for Jan. 14 and 17. Each pixel is associated with either MYI or one of the FYI categories, yielding an ice category spatial frequency distribution, f_i, where i = 1:6 represents the 6 ice categories. The f_i (Table 1) vary with time but are assumed to be constant between the times of the major FYI formations given in Table 1. For instance, the f_i from the Jan. 14 image are different than those from the Jan. 17 image, but are assumed to be constant between 00 UTC Jan. 11 and 00 UTC Jan. 16. Since each FYI pixel has a specific formation time (see Table 1), distributions of ice thickness and snow depth can then be obtained using the 1-D model (see below).

The 1-D snow/ice model was run independently on each of these FYI types and the MYI from the time they were first observed [with an assumed ice thickness of 3 cm when they were first observed], producing continuous estimates of ice thickness, snow depth, and T_s. Observations of snow depth and precipitation at the SHEBA site suggest that there was no snow accumulation from YD344 (Dec. 10) until after YD387 (Jan. 22) (Fig. 1); however, we have assumed that drifting

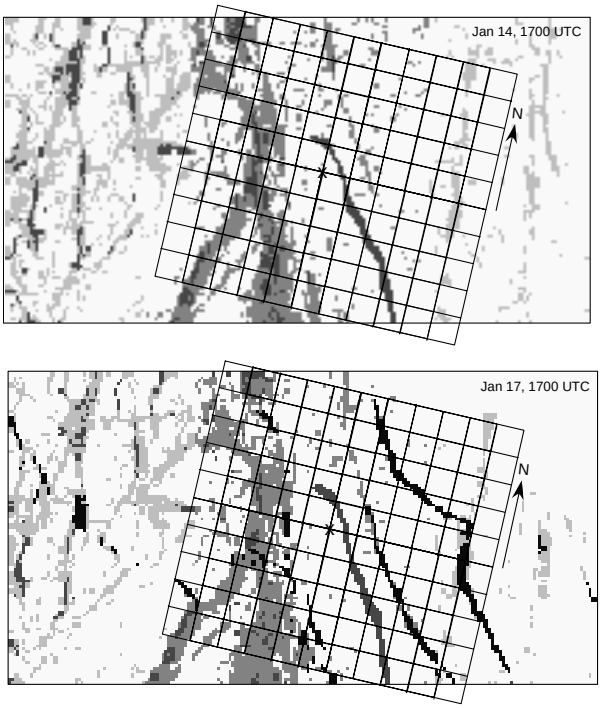

Fig. 7: Spatial distribution of FYI and MYI groups from SAR image classifications from a) YD14 17 UTC and b) YD17 17 UTC with the FYI regions FYI0 (light grey), FYI1(medium grey), FYI2 (dark grey), and FYI3 (black) shaded (also see Table 1). A 100 X 110 km grid around the SHEBA ship (x) is shown. Each small grid is 10 X 10 km. The classifications have been done on 1x1 km areas.

produced 2 cm of snow on each FYI region shortly after it formed. This may be an overestimate and may have led to slightly thinner FYI and colder T_s than would otherwise have been present. Note in Table 1 that the ice thickness for FYI0, which had 10-11 cm of snow on it, grew slower than FYI1, which only had the assumed 2-3 cm of snow.

3.2 Surface Temperatures and Fluxes

The model output show that large spatial variability in ice thickness, T_s, and H_s exists on most days. For example, on YD381 at 02 UTC (AVHRR histogram time of Overland et al. 2000) when four FYI groups and one MYI group were present, the ice thickness varies from 0.04 to 2.13 m (Fig. 8a), the snow thickness varies from 2 cm to 23 cm (Table 1), the surface temperature varies from -19°C to -38°C (Fig. 8b), and the sensible heat flux varies from -19 W m^{-2} over the MYI to +115 Wm^{-2} over FYI3 (Fig. 8c). Note that the T_s spatial variations decrease during the warm periods, which correspond to the cloudy periods (Persson et al. 1999), though the H_s variations aren't always reduced at cloudy times since clouds are frequently associated with storms, which in turn produce stronger winds.

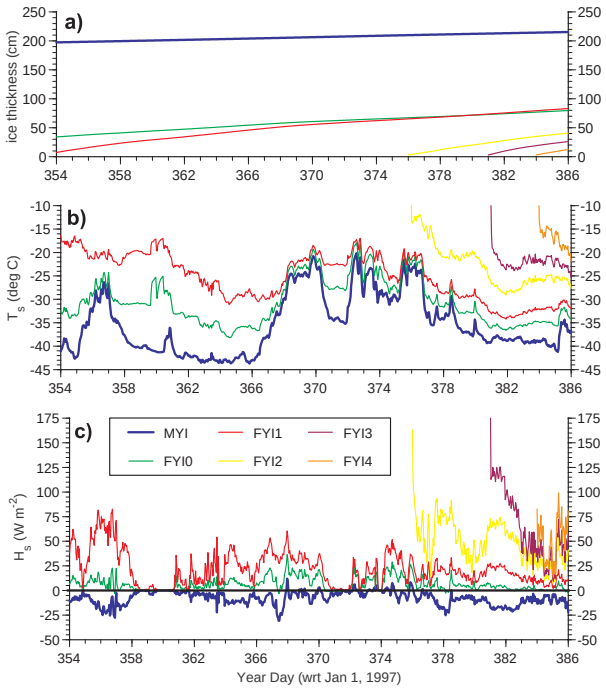

Fig. 8: Model output time series of a) ice thickness, b) surface temperature, and c) H_s over the one MYI site and the 5 FYI groups near the SHEBA location. The beginning of each FYI curve shows when that FYI group formed.

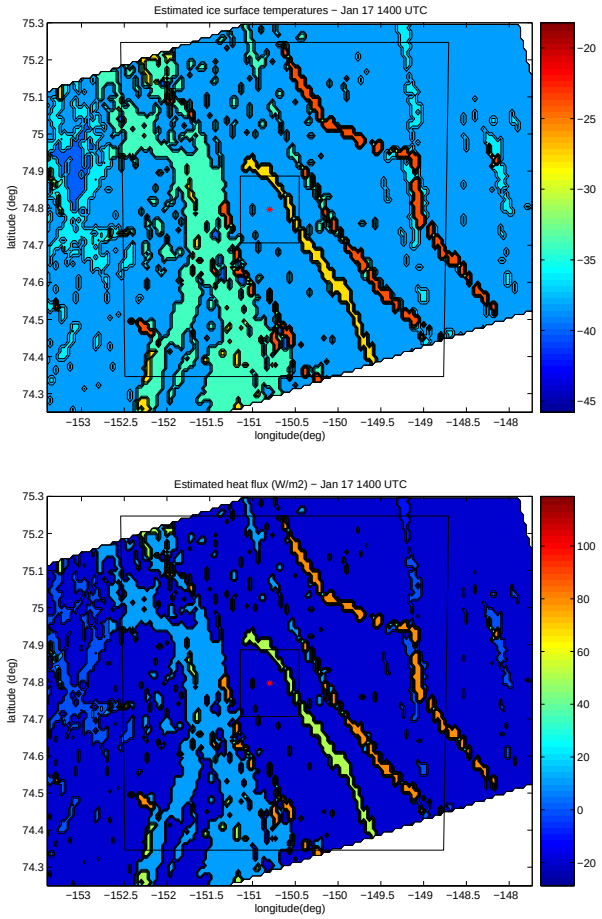

Fig. 9: Spatial distribution of a) T_s and b) H_s at 14 UTC Jan. 17 resulting from the SAR classifications at 17 UTC Jan. 17 and the 1-D snow/ice model. The small box is 20X20 km centered on the SHEBA site, while the large box is the 100X110 km domain shown in Fig. 7 and to be used later in the aggregation and 3-D modeling.

Substituting the modeled T_s and H_s into the ice-classification maps from the SAR data produces spatial maps of each of these parameters for any time (Fig. 9). AVHRR estimates of T_s from clear-sky periods with 1.25 km resolution (Fig. 10) show surface temperatures with the same spatial pattern as obtained from the SAR/1-D model technique. Hence, the spatial variability of snow depth and ice thickness leads to large spatial differences in T_s and H_s.

However, the magnitude of the spatial variability of T_s is larger in the observed AVHRR image (~24°C) compared to that generated from the SAR images and the 1-D model (~15°C). This greater spatial variability is partly due to T_s on parts of the MYI that are up to 6°C colder than the T_s at the SHEBA site. This T_s variability on the MYI isn't captured by our SAR/1-D model technique. There are also details in the AVHRR images not

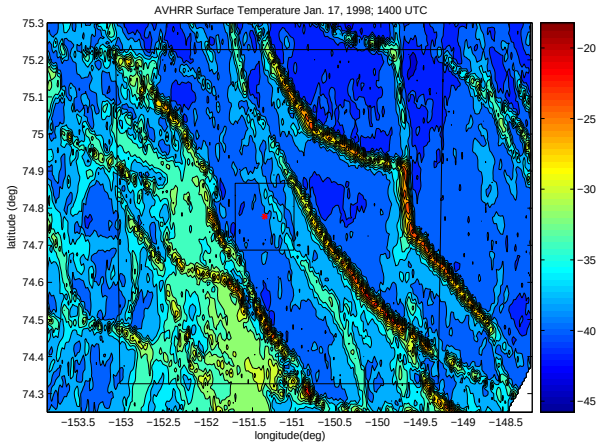

Fig. 10: Observed AVHRR surface temperature at 14 UTC Jan. 17, which was a clear-sky period.

captured by our technique, and we know that the model has a slight cold bias during clear-sky periods.

Though the magnitude of the spatial variability of T_s is underestimated by 35-40% with the SAR/1-D model, this technique clearly captures the main spatial variability pattern in the observed T_s and permits us to determine T_s under both cloudy and clear conditions. Also, because the T_s variability is large and some of the T_s regions have length scales greater than 10 km, the area surrounding the SHEBA site has the potential for producing shallow mesoscale circulations (e.g., Roy and Avissar 2000). Both the variations in T_s and any induced mesoscale circulations will impact the surface fluxes on the GCM scale (approx. 100 X 100 km^2 scale).

4. AGGREGATE TEMPERATURES

To obtain a time series of the aggregate T_s ($\langle T_s \rangle$) from the SAR/1-D technique within the 100 X 110 km box (referred to as domain D1) in Fig. 9a, we compute

$$\langle T_s \rangle (t) = \sum_{i=1}^{6} f_i T_{si}(t) \qquad (2)$$

for all times (YD354-386) for which we have the f_i, where $T_{si}(t)$ is the 1-D model surface temperature at any given time t on ice category i. The time series of $\langle T_s \rangle$ is consistently 0.5-4.0°C warmer (averaging 2.0°C) than the modeled T_s for the MYI, with the difference being 0.5-1.0°C during cloudy periods and 2-4°C during clear-sky periods(Fig. 11). Because FYI1 occupies 14-19% of D1 (Table 1), $\langle T_{s\_SAR/1D} \rangle$ is substantially greater

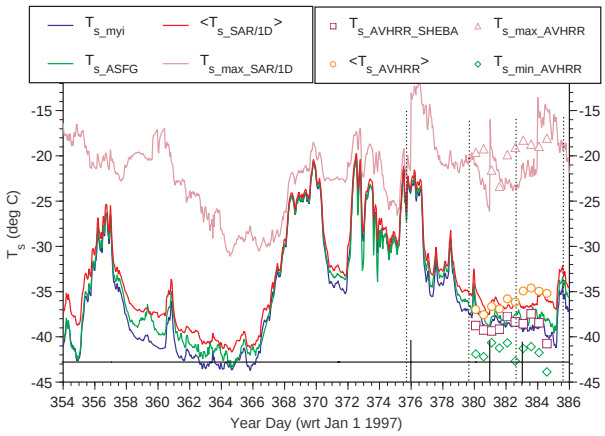

Fig. 11: Aggregate T_s from the SAR/1D method (red line) and the clear-sky AVHRR measurements (brown circles). Also shown are the T_s from the MYI using the 1-D model (blue line), the observed T_s at the ASFG SHEBA site (green line), T_s from the AVHRR at the SHEBA pixel (red squares), maximum T_s from the SAR/1D model (on the thinnest ice) (purple line), and the maximum and minimum T_s from the AVHRR measurements (purple triangles and green diamonds, respectively). Times of the SAR images used for the classifications are shown as vertical dotted lines, and the times of change of the relative fraction values (f_i) are shown as vertical black bars on the horizontal black line.

than T_{s_MYI} for the entire period from YD354. For the clear-sky AVHRR image times between YD380-384, the $\langle T_{s\_AVHRR}\rangle$ - $T_{s\_AVHRR\_SHEBA}$ = 2.8°C while $\langle T_{s\_SAR/1D}\rangle$ - T_{s_MYI} = 2.5°C, showing that the aggregate differences between the two methods are very similar. $T_{s\_AVHRR\_SHEBA}$ is the T_s at the AVHRR pixel at the SHEBA site. Hence, we conclude that the temporally averaged aggregate T_s from the AVHRR measurements overestimate the true difference between aggregate and MYI T_s values because of only considering clear-sky conditions.

Figure 11 also shows that the warmest $T_{s\_SAR/1D}$ is approximately the same as the warmest T_{s_AVHRR}, while the coldest $T_{s\_SAR/1D}$ (that for the MYI) is slightly warmer than the coldest T_{s_AVHRR}, as discussed previously. Note that the clear-sky $T_{s\_AVHRR\_SHEBA}$ are about 1.1°C colder than the coincident observed T_{s_ASFG} and very similar to the T_{s_MYI}, which we know is biased slightly cold from section 2.

5. AGGREGATE SENSIBLE HEAT FLUXES

Flux parameterizations, including the 1-D model, usually predict sensible heat flux (H_s) using the bulk-aerodynamic method, in which

$$H_s = \rho_a\, c_p C_H S \left(T_s - \theta_r\right). \qquad (3)$$

Here T_s is the surface temperature; θ_r, the average potential temperature at reference height r; and S a velocity scale that represents the wind speed and the gustiness. The heart of the bulk-aerodynamic method is finding the transfer coefficients C_H, which depend on the reference height r and on the local stability.

The area-averaged, or aggregate, H_s over a heterogeneous surface can be represented as

$$\left\langle H_s \right\rangle = \sum f_i H_{si} = \sum f_i \rho_{ai}\, c_p C_{Hi} S_i \left(T_{si} - \theta_{ri}\right). \qquad (4)$$

Here H_{si} is the flux over the *i*th surface type, which covers a fraction f_i of the grid, and S_i, T_{si}, and θ_{ri} are versions of the quantities in (3) averaged over the *i*th surface type. $\langle H_s\rangle$ is the desired quantity, but, unfortunately, we generally don't know the properties at the individual surface forms, so (4) can frequently not be evaluated directly.

However, with the assumption that the wind speed (S = u), θ_r, and ρ_a are the same in the entire domain D1 as they are over the MYI at the SHEBA site, and that the C_H (= $\hat{C}_H$) is known, we can compute an estimate of the aggregate $\langle H_s\rangle$ over D1 in a manner similar to that done for $\langle T_s\rangle$. Namely,

$$\begin{aligned} \left\langle H_s \right\rangle' &= \sum_{i=1}^{6} f_i H_{si}' \\ &= c_p \hat{C}_H \rho_a u \sum_{i=1}^{6} f_i \left(T_{si} - \theta_r\right) \\ &= c_p \hat{C}_H \left\langle \rho_a \right\rangle \langle u \rangle \left(\langle T_s \rangle - \langle \theta_r \rangle\right), \end{aligned} \qquad (5)$$

Where the $\langle T_s\rangle$ results from (2) and $\langle \rho_a\rangle$,$\langle u\rangle$, and $\langle \theta_r\rangle$ result from our assumption of uniform atmospheric conditions over D1. If we furthermore assume that $\hat{C}_H$ = C_{H_MYI}, we can then compute $\langle H_s\rangle$'. This is the "mixture" method of aggregation. We can also use the "simple mosaic" method of aggregation by assuming that the C_{Hi} are different but retaining the assumption of uniform atmospheric conditions, leading to

$$\begin{aligned} \left\langle H_s \right\rangle'' &= \sum_{i=1}^{6} f_i H_{si}'' \\ &= c_p \left\langle \rho_a \right\rangle \langle u \rangle \sum_{i=1}^{6} f_i \hat{C}_{Hi} \left(T_{si} - \langle \theta_r \rangle\right) \end{aligned} . \qquad (6)$$

In using (6), we can either assume a constant C_{Hi} for all FYI (e.g., C_{Hi} =1 X 10^{-3} for i = 1-5; C_{Hi}=C_{H_MYI}

for i = 6) that is greater than that over the MYI, as discussed earlier and done by Overland et al. (2000). We can also calculate the C_{Hi} for each ice type allowing the local stability to influence its value. This latter method is typically considered incorrect for narrow leads and FYI because the physical mechanisms that lead to enhanced mixing in unstable regions (i.e., roll vortices, large eddies) require heterogeneity with spatial scales ~10 km in order to develop. However, both the SAR/1-D model method and the AVHRR data show that such scales do exist in parts of D1 (Figs 9 & 10). Hence, this second application of (6) is justified in this case. We will refer to the two methods using (6) as (6a) and (6b), respectively, and the results as $\langle H_s \rangle''_a$ and $\langle H_s \rangle''_b$, respectively.

To be temporally consistent in applying (5), (6a), and (6b), we use the H_{si} from the 1-D model runs that have the appropriate assumptions regarding the C_{Hi}. Since the T_{si} are not independent of the assumption regarding C_{Hi}, the T_{si} time series are different for the different C_{Hi} assumptions when the aggregate H_s are computed. For example, we can apply a $C_{Hi} = 1 \times 10^{-3}$ in the aggregation only if we use the T_{si} time series generated by an assumption of $C_{Hi} = 1 \times 10^{-3}$. This restriction is placed on us when computing the aggregate values because we are physically interpreting the cause of the spatial distribution of T_s as seen in Figs. 9a and 10. This restriction is not present if an aggregate value is computed from a given spatial T_s distribution without regard for consistency with the physical mechanisms creating it, such as done using AVHRR images by, for example, Overland et al. (2000).

Figure 12 shows the time series of $\langle H_s \rangle'$ using (5) between YD354-386. The difference $\langle H_s \rangle' - H_{s\_MYI}$ varies from 0 - 18 W m^{-2} during this time, averaging 6.2 W m^{-2}. While Overland et al.'s (2000) conclusion that the aggregate or regional fluxes tend toward zero during clear-sky periods appears corroborated, this is not the case during cloudy conditions when the H_{s_MYI} can be zero or even positive (e.g., YD369 or YD376; see Fig. 11 for times of cloudy periods, which are coincident with the warm periods). This study instead suggests that the aggregate H_s are equal to or greater than the H_{s_MYI} at all times, and that they can be greater during even the cloudy periods.

Figure 12b and Table 2 show that aggregation methods (6a) and (6b) only increase aggregate flux slightly over that obtained from method (5). The differences $\langle H_s \rangle''_a - H_{s\_MYI}$ and $\langle H_s \rangle''_b - H_{s\_MYI}$ average only 6.8 W m^{-2} and 9.1 W m^{-2}, respectively. For the hours from which AVHRR images were obtained by Overland et al.

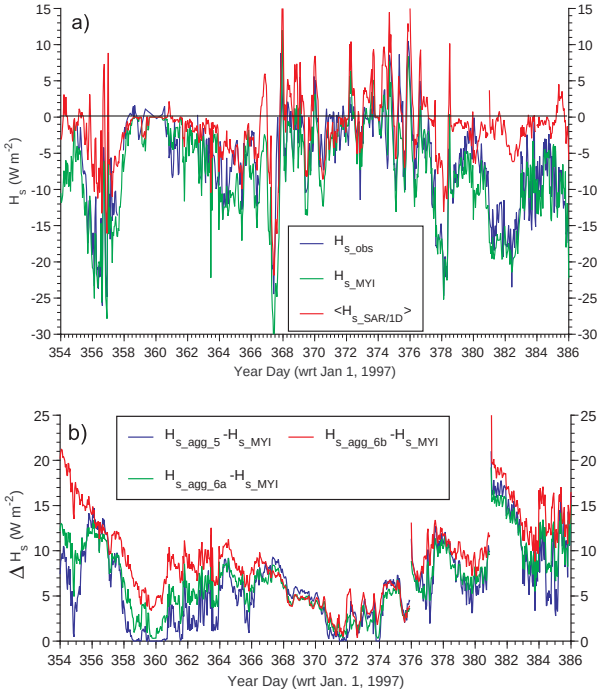

Fig. 12: a) Time series of hourly H_s from observations at the ASFG MYI site (blue), 1-D model at the MYI site (green), and the aggregate value over D1 from the SAR/1-D model technique(red). Panel b) shows the differences $\langle H_s \rangle' - H_{s\_MYI}$ (blue), $\langle H_s \rangle''_a - H_{s\_MYI}$ (green), and $\langle H_s \rangle''_b - H_{s\_MYI}$ (red).

Table 2: *MYI and aggregate H_s (W m^{-2}) for different periods and sources. The second and third rows only use hourly data on the hours from which clear-sky AVHRR images are available (typically 02 and 14 UTC each day). Rows one and two contain the values from our SAR/1D method (except H_{s_ASFG}) and row three contains the values from the AVHRR images done by Overland et al. (2000).*

Period	H_{s_ASFG}	H_{s_MYI}	$\langle H_s \rangle'$	$\langle H_s \rangle''_a$	$\langle H_s \rangle''_b$
YD354-386 (SAR/1D)	-6.0	-7.6	-1.4	-0.8	+1.5
AVHRR(YD378-385)(SAR/1D)	-------	-12.5	-1.7	-1.6	+1.1
O2000(YD378-385)(AVHRR)	-10.6	-------	-0.2	+3.5	------

Table 3: *Mean T_{si} (°C), H_{si} (W m^{-2}), and C_{Hi} (X 10^{-3}) for the MYI and the five FYI categories obtained for the three different aggregation methods. The means are computed from the later of YD354 and when the FYI category formed (see Table 1) through YD385, so the values for FYI2, FYI3, and FYI4 are not comparable to other categories. The focus is on the inter-method comparisons.*

Method/Var	MYI	FYI0	FYI1	FYI2	FYI3	FYI4
5 / T_{si}	-35.1	-30.4	-25.1	-22.9	-22.1	-17.1
5 / H_{si}	-7.4	+6.3	21.8	48.9	64.4	52.2
5 / C_{Hi}	0.79	0.79	0.79	0.93	0.88	0.71
6a / T_{si}	-35.1	-30.7	-26.0	-23.2	-22.5	-19.6
6a / H_{si}	-7.4	+6.8	25.4	50.5	67.7	64.6
6a / C_{Hi}	0.79	1.00	1.00	1.00	1.00	1.00
6b / T_{si}	-35.3	-31.2	-28.5	-27.0	-27.1	-24.9
6b / H_{si}	-7.6	+8.5	36.2	75.0	105.5	115.6
6b / C_{Hi}	0.72	1.64	2.21	1.96	1.99	2.21

(2000), aggregate flux differences from our SAR/1D technique averaged 10.8 W m^{-2}, 10.9 W m^{-2}, and 13.6 W m^{-2} for methods (5), (6a), and (6b), respectively. Overland et al. (2000), when applying the assumption of C_H=C_{H_MYI} (equivalent to method 5), obtained differences of 10.4 W m^{-2} with the reference H_{s_ASFG}, in excellent agreement with our results. However, when applying the assumption in method (6a), they obtained a difference of 14.1 W m^{-2}, which is much greater than the difference we obtained for the same assumption and the same time. Overland et al. did not attempt method (6b).

The reason why the increases in <H_s> from mosaic method (6) compared to the mixture method (5) for our SAR/1D technique were much smaller compared to Overland et al.'s AVHRR application is because the assumptions that increased the C_{Hi} also produced colder T_{si} (Table 3). The increased H_{si} produced a greater surface heat loss and a different surface energy balance in (1), leading to colder surface temperatures and thicker ice. As a feedback, these colder T_{si} reduced the air-surface temperature gradient, resulting in increases in H_{si} that are proportionately much smaller than would be expected from the increases in C_{Hi}.

For method (6b), the decrease in T_{si} is so significant that the maximum T_{si} from this assumption is much colder than the maximum observed T_{S_AVHRR} (Fig. 13). Assuming that the ages of the various FYI areas are reasonably correct and that the 1-D model works reasonably (as was shown in section 2), we must therefore conclude that computing the C_{Hi} from the local stability is not appropriate, despite the presence of large areas of FYI. The differences in the maximum T_s from methods (5) and (6a) are small enough that we are not able to conclude that either method is superior to the other.

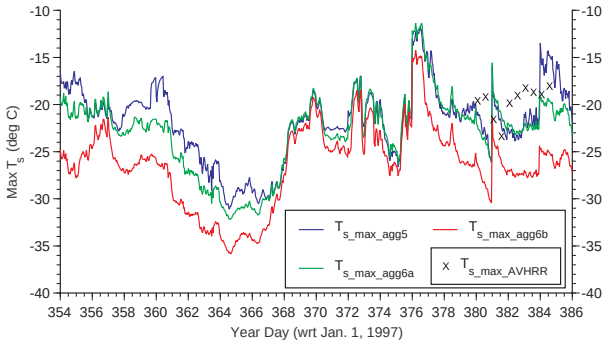

Fig. 13: Maximum T_s within domain D1 using the SAR/1D method for H_s computation method (5) (blue), (6a) (green), and (6b) (red). The maximum T_s from the AVHRR images are given by "x".

5. DISCUSSION AND CONCLUSIONS

We have devised a method for obtaining the spatial distribution of ice surface temperature, surface sensible (and latent) heat fluxes, snow depth and ice thickness on the Arctic pack ice. This method relies on a simple 1-D snow and ice model and on the ability to assign a formation time to any pixel identified as being FYI using SAR data. Validation shows that the 1-D model and this SAR/1D method both produce reasonable and consistent results, and we feel confident that we could extend our analysis backwards in time to the start of the SHEBA data set (late October 1997). However, extending it forward beyond the end of January may be difficult, since the complex

deformations of the pack ice make it cumbersome to use the semi-subjective technique for identifying various FYI categories and assigning formation dates. Modifications of current techniques to assess FYI formation and deformation (e.g., Kwok and Cunningham 2002; Lindsay 2002) by tracking the shape and size of a polygon of a few tens of kilometers on a side on SAR images could perhaps be modified to obtain FYI formation dates on a 1X1 km scale.

The method developed allows us to estimate the aggregate T_s and H_s (as well as other parameters) over a GCM-scale grid surrounding the SHEBA site during a month-long period on an hourly basis for both clear and cloudy conditions. The red curve in Fig. 12a shows the best estimate for the aggregate H_s. It averages 6.2 W m^{-2} greater than the simultaneous H_s on the MYI, as seen in Table 2. This difference is less than the 10-12 W m^{-2} difference suggested by most of the AVHRR assessments by Overland et al. (2002). Table 2 shows that our method also obtains these larger differences if we restrict our analysis to the clear-sky times of the AVHRR measurements. However, Fig. 12 shows that the aggregate H_s are typically greater than the MYI values for both cloudy and clear conditions.

A consistent application of three different assumptions regarding the heat transfer coefficient (C_H) in the 1-D model and the aggregation methods has suggested that the computation of C_H based on local stability is inappropriate because the resulting T_s are too cold. The differences in the aggregate H_s between the other two assumptions are much smaller than suggested by static aggregation applications to a given spatial T_s distribution.

The SAR/1D technique is also capable of providing spatial fields of snow depth and ice thickness. Such fields are needed as a lower boundary condition to 3-D mesoscale models. The heterogeneity in these two parameters produces the large variability in T_s, which in turn may produce mesoscale circulations in the atmospheric boundary layer. Simulations should be able to ascertain whether such circulations exist and how much they contribute to aggregate-scale surface sensible heat fluxes.

Acknowledgments

The author acknowledges the hard work by numerous people in collecting, processing, and analyzing the various SHEBA data sets used in this work. This includes (but is not limited to): T. Grenfell, T. Horst, J. Intrieri, R. Kwok, B. Light, J. Maslanik, R. Moritz, D. Perovich, J. Richter-Menge, M. Shupe, and T. Uttal. This work has been supported by NSF grant OPP-0084322.

6. REFERENCES

Andreas, E. L., 1987: A theory for the scalar roughness and the scalar transfer coefficients over snow and sea-ice. *Boundary Layer Meteorol*., **38**, 159-184.

Beljaars, A. C. M., and A. A. M. Holtslag, 1991: Flux parameterization over land surfaces for atmospheric models. *J. Appl. Meteor*., **30 (3)**, 327-341.

Ebert, E. E., and J. A. Curry, 1993: An intermediate one-dimensional thermodynamic sea ice model for investigating ice-atmosphere interactions. *J. Geophys. Res.*, **98**, C6, 10,085-10,109.

Fairall, C. W., E. F. Bradley, J. E. Hare, A. A. Grachev, and J. B. Edson, 2003: Bulk parameterization of air-sea fluxes: Updates and verification for the COARE algorithm. *J. Clim*., **16**, 571-591.

Fairall, C. W., E. F. Bradley, D.P. Rogers, J.B. Edson, and G.S. Young, 1996: Bulk parameterization of air-sea fluxes for TOGA-COARE. *J. Geophys. Res.*, **101**, 3747-3764.

Fetterer, F. M., D. Gineris, and R. Kwok, 1994: Sea ice type maps from Alaska Synthetic Aperture Radar Facility imagery: An assessment. *J. Geophys. Res*., **99**, C11, 22,443-22,458.

Grachev, A. A., E. L Andreas, C. W. Fairall, P. S. Guest, and P. O. G. Persson, 2004: The SHEBA profile functions in the stable atmospheric boundary layer. *Boundary-Layer Meteor*., in preparation.

Intrieri, J. M., M. D. Shupe, T. Uttal, and B. J. McCarty, 2002: An annual cycle of arctic cloud characteristics observed by radar and lidar at SHEBA. *J. Geophys. Res*., **107**, C10, 10.1029/2000JC000423.

Kwok, R., E. Rignot, and B. Holt, 1992: Identification of sea ice types in spaceborne synthetic aperture radar. *J. Geophys. Res*., **97**, C2, 2391-2402.

Kwok, R., and G. F. Cunningham, 1994: Backscatter characteristics of the winter ice cover in the Beaufort Sea. *J. Geophys. Res*., **99**, C4, 7787-7802.

Kwok, R., D. A. Rothrock, H. L. Stern, and G. F. Cunningham, 1995: Determination of the age distribution of sea ice from Lagrangian observations of ice motion. *IEEE Trans. Geosci. Remote Sens*., **33** (2), 392-400.

Kwok, R., and G. F. Cunningham, 2002: Seasonal ice area and volume production of the Arctic Ocean: November 1996 through April 1997. *J. Geophys. Res*., **107**, C10, 8038, doi:10.1029/2000JC000469.

Lindsay, R. W., 2002: Ice deformation near SHEBA. *J. Geophys. Res*., **107**, C10, 8042, doi:10.1029/2000JC000445.

Maykut, G. A., and N. Untersteiner 1969: Numerical prediction of the thermodynamic response of sea

ice to environmental changes. The Rand Corporation, Santa Monica, Calif., RM-6093-PR.

Overland, J. E, S. McNutt, J. Groves, S. Salo, E. L. Andreas, and P. O. G. Persson, 2000: Regional sensible and radiative heat flux estimates for the winter Arctic during SHEBA. *J. Geophys. Res*., **105 (C6)**, 14,093-14,102.

Perovich, D. K., T. C. Grenfell, J. A. Richter-Menge, B. Light, W. B. Tucker III, and H. Eicken, 2003: Thin and thinner: Sea ice mass balance measurements during SHEBA. *J. Geophys. Res.*, **108**, C3, 8050, doi:10.1029/2001/JC001079.

Persson, P. O. G., C. W. Fairall, E. L. Andreas, P. S. Guest, and D. K. Perovich, 2002: Measurements near the Atmospheric Surface Flux Group tower at SHEBA: Near-surface conditions and surface energy budget. *J. Geophys. Res.* **107**(C10), 8045, doi:10.1029/2000JC000705.

Persson, P. O. G., T. Uttal, J. M. Intrieri, C. W. Fairall, E. L. Andreas, and P. S. Guest, 1999: Observations of large thermal transitions during the Arctic night from a suite of sensors at SHEBA. *Preprints, 3rd Symp. on Integrated Observing Systems*., Jan. 10-15, 1999, Dallas, TX, 171-174.

Roy, S. B., and R. Avissar, 2000: Scales of response of the convective boundary layer to land-surface heterogeneity. *Geophys. Res. Lett.*, **27**, 533-536.

Schwarzacher, W., 1959: Pack ice studies in the Arctic Ocean. *J. Geophys. Res.*, **64**, 2357-2367.

Semtner, A. J., Jr., 1976: A model for the thermodynamic growth of sea ice in numerical investigation of climate. *J. Phys. Oceanogr.*, **6**, 379-389.

Stern, H. L., and R. E. Moritz, 2002: Sea ice kinematics and surface properties from RADARSAT synthetic aperture radar during the SHEBA drift. *J. Geophys. Res*., **107**, C10, 8028, doi:10.1029/2000JC000472.

Sturm, M., J. Holmgren, and D. K. Perovich, 2002b: Winter snow cover on the sea ice of the Arctic Ocean at the Surface Heat Budget of the Arctic Ocean (SHEBA): Temporal evolution and spatial variability. *J. Geophys. Res*., **107**, **C10**, 8047, doi:10.1029/2000JC000400.

Sturm, M., D. K. Perovich, and J. Holmgren, 2002a: Thermal conductivity and heat transfer through the snow on the ice of the Beaufort Sea. *J. Geophys. Res*., **107**, **C21**, 8043, doi:10.1029/2000JC000409.

Uttal, T., J. A. Curry, M. G. McPhee, D. K. Perovich, R. E. Moritz, J. A. Maslanik, Peter S. Guest, H. L. Stern, J. A. Moore, R. Turenne, A. Heiberg, M. C. Serreze, D. P. Wylie, O. G. Persson, C. A. Paulson, C. Halle, J. H. Morison, P. A. Wheeler, A. Makshtas, H. Welch, M. D. Shupe, J. M. Intrieri, K Stamnes, R. W. Lindsey, R. Pinkel, W. S. Pegau, T. P. Stanton, and T. C. Grenfeld, 2002: The surface heat budget of the Arctic, *Bull. Amer. Meteor. Soc.*, **83**, 255-275.